








Synthesis and Characterization of $\text{Cu}_2\text{Zn}_{1-x}\text{Ca}_x\text{SnS}_4$ Thin-films by Spin-coating Technique and Numerical Simulation of the Accompanied CZCTS/CZTS Based Solar Cell

Olusola Akinrinola ^{1,*}, Mojinyinola Kofoworola Awodele ¹, Abideen A. Ibiyemi ², Olusesan Abel Olu-Arotiowa ³, Omowunmi Abidemi Akinrinola ¹, George Atilade Alagbe ¹, Ayodeji Oladiran Awodugba ¹

¹ Department of Pure and Applied Physics, Faculty of Pure and Applied Sciences, Ladoké Akintola University of Technology, Ogbomoso, Nigeria; oakinrinola40@lautech.edu.ng (O.A.), mkawodele@lautech.edu.ng (M.K.A.), omowunmiabidemi.akinrinola@gmail.com (O.A.A.), gaalagbe@lautech.edu.ng (G.A.A.), aoawodugba@lautech.edu.ng (A.O.A.);

² Department of Physics, Federal University Oye-Ekiti, Oye-Ekiti, Nigeria; abideen.ibiyemi@fuoye.edu.ng (A.A.I.);

³ Department of Chemical Engineering, Faculty of Engineering and Technology, Ladoké Akintola University of Technology, Ogbomoso, Nigeria; oaolu-arotiowa@lautech.edu.ng (O.A.O.A.);

* Correspondence: oakinrinola40@lautech.edu.ng (O.A.);

Scopus Author ID 57195735050

Received: 28.03.2022; Accepted: 8.05.2022; Published: 10.12.2022

Abstract: $\text{Cu}_2\text{Zn}_{1-x}\text{Ca}_x\text{SnS}_4$ (CZCTS) nanoparticles were grown on pre-cleaned glass substrates using spin-coating. The obtained nanoparticle alloy thin film changed from light green to bluish-green as Ca^{2+} content increased in the alloy. The elemental analysis confirmed the presence of Cu^+ , Zn^{2+} , Ca^{2+} , Sn^{4+} , and S^{2-} ; scanning electron microscopy images exhibited an uneven grain size distribution without cracks or holes. The grain size increases as the Ca^{2+} increases. The X-ray diffraction analysis revealed a polycrystalline alloy nature. The typical peaks indicated from the diffraction by the samples are (100), (200), and (210). The alloy exhibits a simple cubic lattice. The absorption is more significant in the 200 to 400 nm region, which significantly reduces beyond 400 nm. The optimum bandgap energy obtained ranged from 3.84-4.04 eV. CZCTS/CZTS-based thin film solar cells show excellent performance with an open-circuit voltage ~816 mV and overall cell efficiency of ~16.95%, exhibiting commercial potential for large-scale fabrication of photovoltaic devices.

Keywords: CZCTS; nanoparticles; polycrystalline; alloy; thin film; wide band gap.

© 2021 by the authors. This article is an open-access article distributed under the terms and conditions of the Creative Commons Attribution (CC BY) license (<https://creativecommons.org/licenses/by/4.0/>).

1. Introduction

The recent approach to improving photovoltaic cell conversion performance has resulted in a flurry of research into environmentally friendly materials [1-3]. Due to the scarcity and cost implications of their constituents (In, Ga, and Te), recent research interests have moved away from absorber materials like $\text{CuInGa}_{1-x}\text{Se}_2$ (CIGS) and CdTe [4,5]. $\text{Cu}_2\text{Zn}_{1-x}\text{Ca}_x\text{SnS}_4$ (CZCTS) is a new material whose elements have replaced In and Ga with $\text{Zn}_{1-x}\text{Ca}_x$ and Sn in CIGS [4,6]. These elements are readily available and non-toxic thus, makes them environmentally friendly. CZCTS is a quinary substance ($\text{I}_2\text{-II}_{1-x}\text{-II}_x\text{-IV-VI}_4$) with a similar

structure to CIGS [2,5]. Among the many potentials uses for thin-film technology are solar cells, LEDs, transistors, and diodes, to name a few.

Since the photovoltaic effect of CZTS (a sister substance; where Ca^{2+} is zero) was recorded by the sputtering technique [7], other methods have been used to prepare the thin film, including RF magnetron sputtering, vacuum evaporation, SILAR, electrodeposition, spray pyrolysis, non-vacuum process, pulsed laser methods, and so on [7-13].

Research and rapid prototyping have relied on spin coating because of its simplicity, relative ease of setup, and capability to achieve a uniform layer at various thicknesses [14-16]. However, due to the challenges in directly depositing CZTS thin films on a substrate, most experiments on wet chemical techniques have focused on particles rather than thin films. Therefore, there is little information on the effect of deposition of CZTS synthesis via the spin coating method [5,7,12-14]. This deposition approach consists of a few steps: producing CZCTS powder, mixing with a solvent, and coating on a glass substrate.

2. Materials and Methods

2.1. Material preparation, deposition, and characterization.

The substrates were first cleaned with liquid detergents to remove all forms of particles, such as dirt or dust. The substrates were later dipped in acetone and ethanol and sonicated for degreasing (removing organic particles and metal oxides which may be challenging for the detergent to remove). The substrates were then rinsed with deionized water and dried in the oven at room temperature before deposition.

These steps and processes were repeated for all samples. The syntheses required the variation of the relative ratio of Zinc and Calcium ions in $\text{Cu}_2\text{Zn}_{1-x}\text{Ca}_x\text{SnS}_4$ with parameter $0.0 \leq x \leq 1.0$, with a step height of 0.2. The composition x was determined by using Equation 2.1.

$$x = \frac{[\text{Mass of CaSO}_4 \text{ in solution}]}{[\text{Mass of ZnSO}_4 \text{ in solution} + \text{Mass of CaSO}_4 \text{ in solution}]} \quad (2.1)$$

20.00 ml each of 0.1 M of Cu_2SO_4 , ZnSO_4 , SnSO_4 , $\text{Na}_2\text{S}_2\text{O}_3$, and 20.00 ml of x M of CaSO_4 were all mixed in a beaker. 10.00 ml of NH_4OH and $\text{C}_5\text{H}_{15}\text{NO}_3$ were added as complexing agents [15,19]. Each mixture was heated for 90 minutes at 90 °C with a magnetic stirrer. The moles of each precursor and complexing agent were calculated using Equation 2.2, and the values were presented in Table 1.

$$\text{No of moles} = \frac{\text{Mass in grams}}{\text{Molar Mass}} \quad (2.2)$$

The centrifugation separated the residue from the supernate after the solution was stirred and heated for 90 minutes. The deionized water was added and filtered. The residue was dried in an oven at room temperature for four days. The dried samples of $\text{Cu}_2\text{Zn}_{1-x}\text{Ca}_x\text{SnS}_4$ were then kept in clean specimen bottles and labeled. The entire pieces were six in number. 0.1 grams of each material was mixed with 10.00 ml of deionized water in a beaker. The solution is then put on the glass substrate dropwise with a syringe in the spin coater at 3000 rpm for 30 secs. This process was repeated for all six samples. The deposited samples were left to dry in the oven at room temperature. The deposited thin-film samples of $\text{Cu}_2\text{Zn}_{1-x}\text{Ca}_x\text{SnS}_4$ were studied using X-Ray Diffractometer (XRD), Scanning Electron Microscope (SEM), and Energy Dispersive X-ray (EDX), UV-VIS spectrophotometer for structural analysis, surface morphology, and optical characteristics.

Table 1. Parameters for the Synthesis of $\text{Cu}_2\text{ZnCaSnS}_4$ concentrations.

Compounds	x	CaSO_4 (mol)	$\text{Zn}(\text{NO}_3)_2$ (mol)	Cu_2SO_4 (mol)	SnSO_4 (mol)	$\text{Na}_2\text{S}_2\text{O}_3$ (mol)	NH_4OH (mol)	$\text{C}_5\text{H}_{15}\text{NO}_3$ (mol)
$\text{Cu}_2\text{Zn}_{1.0}\text{Ca}_{0.0}\text{SnS}_4$	0.00	0.000	0.100	0.100	0.100	0.100	0.100	0.100
$\text{Cu}_2\text{Zn}_{0.8}\text{Ca}_{0.2}\text{SnS}_4$	0.20	0.025	0.100	0.100	0.100	0.100	0.100	0.100
$\text{Cu}_2\text{Zn}_{0.6}\text{Ca}_{0.4}\text{SnS}_4$	0.40	0.067	0.100	0.100	0.100	0.100	0.100	0.100
$\text{Cu}_2\text{Zn}_{0.4}\text{Ca}_{0.6}\text{SnS}_4$	0.60	0.150	0.100	0.100	0.100	0.100	0.100	0.100
$\text{Cu}_2\text{Zn}_{0.2}\text{Ca}_{0.8}\text{SnS}_4$	0.80	0.400	0.100	0.100	0.100	0.100	0.100	0.100
$\text{Cu}_2\text{Zn}_{0.0}\text{Ca}_{1.0}\text{SnS}_4$	1.00	0.100	0.000	0.100	0.100	0.100	0.100	0.100

2.2. Numerical simulations.

Solar cell Capacitance Simulator (SCAPS-1D) was used to simulate the solar cells as $\text{Cu}_2\text{Zn}_{1-x}\text{Ca}_x\text{SnS}_4$ is employed as an absorber layer. The optoelectronics parameters were derived from the characterization, and the same were used as input parameters in SCAPS- 1D. The optoelectronic parameters [5,20-24] used in the simulation are described in Table 2. The optoelectronic parameters used were all determined from the synthesis and characterization, and where such could not be derived, the same was taken from a cited experimental study in literature with reasonable estimates in some cases [25-27]. The cell structure used in the simulation is p-CZTS/n-ZnO/n-CZCTS/n-FTO.

Table 2. The optoelectronic parameters of the materials used for the simulations.

Parameters	CZTS	CZCTS	FTO
Band Gap (eV)	1.56	3.86	3.60
Density of States - N_C (cm^{-3})	2.20×10^{18}	$2.2 \times 10^{12} - 2.2 \times 10^{22}$	1.2×10^{20}
Density of states - N_V (cm^{-3})	1.80×10^{19}	1.6×10^{19}	7.0×10^{20}
Electron affinity (eV)	4.21	4.95	4,50
Electron mobility ($\text{cm}^2.\text{V}^{-1}.\text{s}^{-1}$)	1.00×10^2	25	20
Hole mobility ($\text{cm}^2.\text{V}^{-1}.\text{s}^{-1}$)	2.00×10^1	100	100
Free Carrier Concentration N_A (cm^{-3})	4.00×10^{16}	0	0
Free Carrier Concentration N_D (cm^{-3})	0	$10^{15} - 10^{23}$	3.5×10^{20}
Relative permittivity	10.00	9.00	10.00
Thickness (μm)	2.00	0.01 - 0.05	0.0125

3. Results and Discussion

3.1. Structural properties of the $\text{Cu}_2\text{Zn}_{1-x}\text{Ca}_x\text{SnS}_4$.

The X-ray diffraction spectra of the six samples at the variation of Ca^{2+} and Zn^{2+} are revealed. The effect of Ca^{2+} and Zn^{2+} ions on the thin-film samples are presented in Figure 1. The diffraction pattern obtained from the XRD exhibited a polycrystalline nature. It is revealed here that the diffraction peaks disappear as the Zn^{2+} content in the sample increases. Also, the peaks resurfaced when both Zn^{2+} and Ca^{2+} were nearing even compositions. The common peaks revealed from the diffraction by the samples are (100), (200), and (210). These three peaks are the preferential orientation for the alloy - $\text{Cu}_2\text{Zn}_{1-x}\text{Ca}_x\text{SnS}_4$. Others are; (110), (111), (211), (300), (310), (320), (331), (332), (333), (400), (411), (421), (522), (531), and (921). Most of these peaks emerged when Ca^{2+} was so pronounced in the alloy.

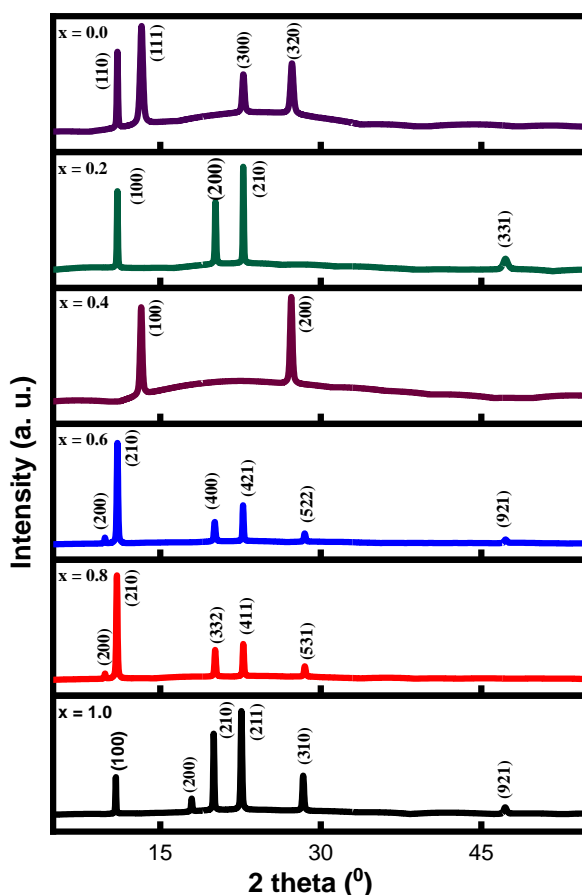


Figure 1. XRD spectra pattern of $\text{Cu}_2\text{Zn}_{1-x}\text{Ca}_x\text{SnS}_4$ for $0.0 \leq x \leq 1.0$.

The alloy exhibits a simple cubic lattice. There is a consistent linear decrease in lattice constant as Ca^{2+} increases in the alloy but peaked at 0.6-mole fraction after that decreases as the Ca^{2+} increases. The interplanar spacing seems to be in the same order throughout each sample. There is a sharp decrease in particle size as Ca^{2+} is introduced into the alloy. The particle size is not affected by continuous additions. The lower the magnitude of the particle, the larger the surface area. It is essential to charge carrier mobility which will, in turn, affect the conductivity within the alloy. A grain size with a large particle magnitude exhibits a relatively small surface band reflecting a lower surface area. The modified Scherrer formula and Williamson-Hall method (Equation 3.1) was used to obtain the crystallite size and microstrain [28,29].

$$\beta \cos \theta = \frac{k\lambda}{\tau} + 4\varepsilon \sin \theta \quad (3.1)$$

where, τ is the mean size of the ordered crystalline domain, k is the dimensionless shape factor known as Scherrer's constant with a value of 0.9, β is the full width at half maxima of the XRD peak, θ is the Bragg's diffraction angle, λ is the wavelength of X-ray, and ε represents the microstrain. The average crystallite size and microstrain of the CZTS nanostructures are presented in Table 3. Other parameters presented in Table 2 are the dislocation density (Equation 3.2), stacking factor (Equation 3.3), and atomic percentage composition of calcium (Equation 3.4) in the alloy [28,30,31].

Table 3. Shown % composition of Ca, crystallite size, microstrain, dislocation and stacking factor.

x	% composition of Ca	Crystallite size (nm)	Microstrain	Dislocation density	Stacking factor
0.00	0.00	26.700	0.1996	1.613	0.655
0.20	2.31	34.530	0.4037	1.519	0.589
0.40	5.58	15.780	0.1301	1.034	0.638
0.60	8.43	31.645	2.2932	0.656	0.629
0.80	11.21	39.064	0.1091	0.691	0.662
1.00	14.15	49.130	3.5152	0.385	0.515

$$\text{dislocation density} = \frac{1}{D^2} \tag{3.2}$$

$$\text{stacking factor} = \left[\frac{(2\pi)^2}{45(3 \tan \theta)^2} \right] \tag{3.3}$$

$$\% \text{ composition of Ca in the alloy} = \left[\frac{(\text{Ca})}{(\text{Ca}+\text{Zn})} \right] \times 100 \text{ (mol\%)} \tag{3.4}$$

The dislocation density (line defect) in this alloy is a linear crystallographic defect within the crystal structure that induces an abrupt change in the arrangement of atoms, which affects various properties of this alloy. In this alloy, the introduction of Ca^{2+} increases the dislocation as these ions increase; there is a drop in the size of the dislocation.

3.2. Surface morphology of $\text{Cu}_2\text{Zn}_{1-x}\text{Ca}_x\text{SnS}_4$.

The SEM micrograph images obtained for the thin-film samples are presented in Figure 2. The samples' images show an improvement of coarse grain morphology as Ca^{2+} size reduces (an increase of Zn^{2+}). The grain size is not evenly distributed (though nano-sized) in each sample. The disparity in grain size reduces as the Zn^{2+} ion content increases. The average grain size ranged between 15.78 nm – 44.13 nm.

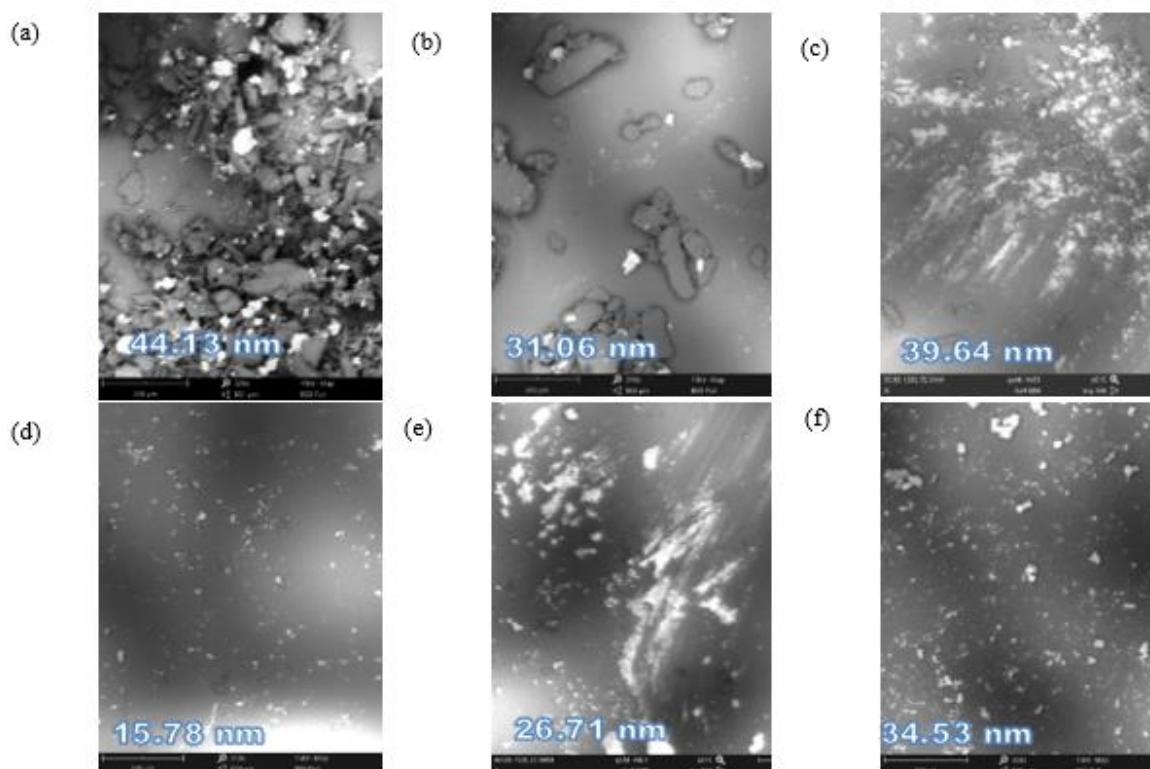


Figure 2. SEM micrographs of $\text{Cu}_2\text{Zn}_{1-x}\text{Ca}_x\text{SnS}_4$ with different content values of x for (a) 1.0 (b) 0.8 (c) 0.6 (d) 0.4 (e) 0.2 and (f) 0.0.

3.3. Optical absorbance and transmittance properties.

The optical absorbance of the alloy; $\text{Cu}_2\text{Zn}_{1-x}\text{Ca}_x\text{SnS}_4$ was obtained via a UV-VIS-IR spectrophotometer. Figure 3 depicts the variation in the alloy along with the wavelength. All the alloys revealed a great deal of absorption as the wavelength increased. The absorption is more significant in regions 200 to 400, which significantly decreases beyond 400 nm. The effect of Ca^{2+} content as it grows in the alloy, as presented in the plots, confirmed the lower absorption in the blue region. It can be inferred that the absorption of the shorter wavelength of the photons may be reduced, mitigating the absorption losses. The optical transmittance, which is the effectiveness of the alloy in transmitting radiant energy, is presented in Figure 4. The plots illustrate the variation of optical transmittance with a wavelength in the region of 200 to 1100 nm. The presence of Ca^{2+} acted as a dopant in the alloy. And this conforms [18,32-34] with the reported 95% transmittance as Zn^{2+} is used to enhance the crystallinity of CdS in solar cell applications [19,34].

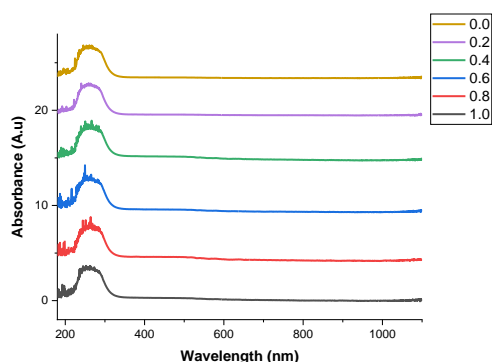


Figure 3. Optical absorption pattern of $\text{Cu}_2\text{Zn}_{1-x}\text{Ca}_x\text{SnS}_4$ thin film for $0.0 \leq x \leq 1.0$.

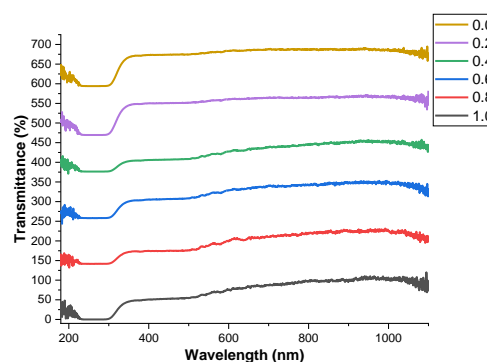


Figure 4. Optical transmittance pattern of $\text{Cu}_2\text{Zn}_{1-x}\text{Ca}_x\text{SnS}_4$ thin film for $0.0 \leq x \leq 1.0$.

3.3. Optical energy bandgap.

Figures 5 and 6 illustrate that the optical band gap specifies how much of the solar spectrum is absorbed by a photovoltaic cell using the alloy.

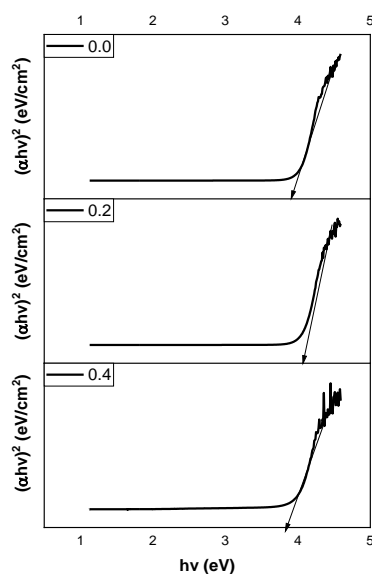


Figure 5. Energy band gaps of $\text{Cu}_2\text{Zn}_{1-x}\text{Ca}_x\text{SnS}_4$ thin film for $0.0 \leq x \leq 0.4$.

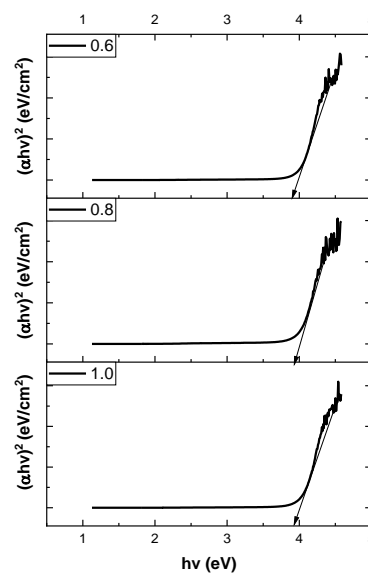


Figure 6. Energy band gaps of $\text{Cu}_2\text{Zn}_{1-x}\text{Ca}_x\text{SnS}_4$ thin film for $0.6 \leq x \leq 1.0$.

This alloy will not absorb photons with less energy than the bandgap, and the energy of the electron-hole pair formed by a photon is equal to this bandgap energy. The variation of Ca^{2+} in the alloy accounts for the different energy gaps obtained. The bandgap presented in the plots is the exciton energy that defines the onset of vertical inter-band transition. The optical bandgap of the alloy varied from 3.84 – 4.04 eV, which makes this alloy a Wide Band Gap (WBG) semiconductor. This energy shift is consistent with the energy gap with the behavior of dopants, as reported in the literature. However, the optical bandgap is at variance with the quaternary $\text{Cu}_2\text{ZnSnS}_4$ alloy [20-22].

3.4. Solar cell performance.

Figure 7 illustrates the J-V curve due to carrier densities. The variation in carrier densities while the density of states - conduction band and valence band were kept at 2.2×10^{12} and $1.8 \times 10^{19} \text{ cm}^{-3}$, respectively, at a constant thickness of 10 nm. The J_{sc} , V_{oc} , FF, and CE increase as the value of carrier density increases [35-37]. The increment continues for all the electrical parameters but fills the factor at $2.2 \times 10^{22} \text{ cm}^{-3}$, as depicted in Figures 8 and 9. The FF increased from 53.63 – 70.84% before dropping to 59.45% at a maximum CE of 16.95%.

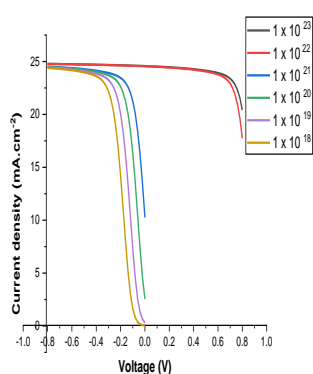


Figure 7. J-V of cells with different carrier densities (cm^{-3}) in the CZCTS buffer layer.

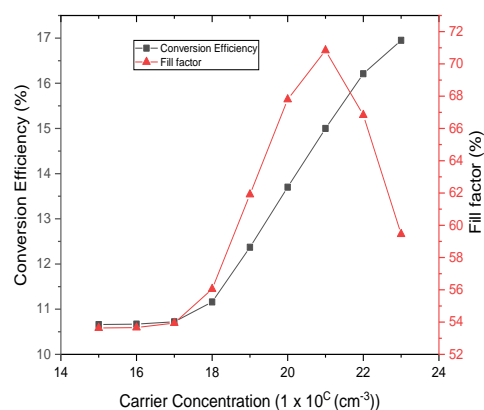


Figure 8. The dependence of cell performance on the carrier concentration of CZCTS Conversion Efficiency and Fill factor.

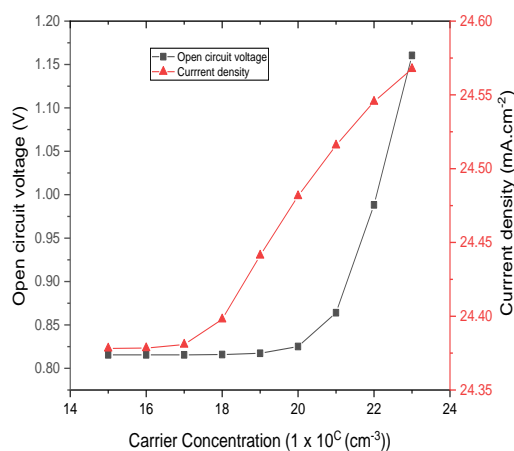


Figure 9. The dependence of cell performance on the carrier concentration of CZCTS Open circuit voltage and current density.

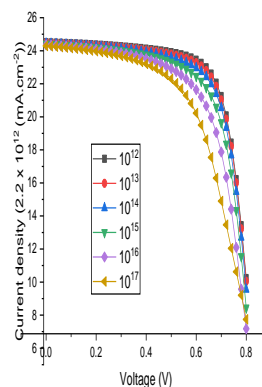


Figure 10. J-V of cells with different carrier densities in the CZCTS buffer layer.

The V_{OC} and J_{SC} increased from 0.8155 – 1.1605 V and 24.3782 – 24.5676 mA.cm⁻² respectively. Figure 10, on the other hand, is the J-V curve due to the density of the state (conduction band). The electrical parameters keep dropping, though the carrier density, density of state (valence band), and thickness were kept constant at 1 x 10²¹ cm⁻³, 1.8 x 10¹⁹, and 10 nm, respectively. Figures 11 and 12, illustrate the dependence of the electrical parameters; the FF, J_{SC} , and CE as it decreases from 70.84 – 32.65%, 24.5156 – 23.6980 mA.cm⁻² and 16.95 – 6.42 % respectively while V_{OC} suddenly peaked at 2.2 x 10¹⁷ cm⁻³ density of state with 0.9059 V before finally decreased to 0.8291 at 2.2 x 10²² cm⁻³.

The simulated thickness of the CZCTS as a buffer layer did not affect this planar arrangement's electrical parameters when the thickness varied from 10–20 nm. It will amount to a share waste of resources when more than 10 nm of this material is being deployed as a buffer material in a PV system. In searching for the best way to optimize the material, its density of state for the conduction band varied from 2.2 x 10¹² - 2.2 x 10²² cm⁻³. The best conversion efficiency (CE) fill factor (FF), open-circuit voltage (V_{OC}), and short circuit current density (J_{SC}) were obtained at 2.2 x 10¹² cm⁻³, as depicted in Figures 11 and 12.

It can be seen that although the increase in density of state (conduction band) resulted in the reduction of J_{SC} , V_{OC} , FF, and CE, the reduction is not as significant for V_{OC} and J_{SC} as that for FF and CE. This phenomenon is attributed to the fact that the density of the state must be kept at a minimum since the buffer layer is ultra-thin. This thinness allows the absorber layer to absorb fewer incident photons, thereby reducing Shockley-Read-Hall recombination at the centers of the buffer layer. However, it is pertinent to avoid a very thin buffer layer (< 10 nm); a reduction of V_{OC} , J_{SC} , and CE may be recorded as a narrow buffer layer may result in leakage current, and too thick one could lead to a low carrier separation rate [38]. From the above, the optimized and preferred buffer layer thickness for this material is 10 nm.

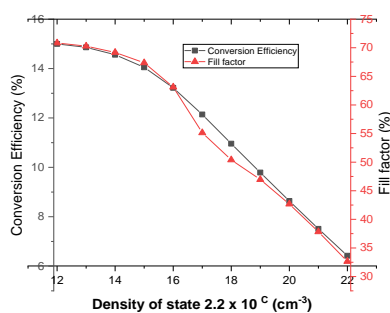


Figure 11. The dependence of conversion efficiency and fill factor on the density of states (conduction band) for the CZCTS.

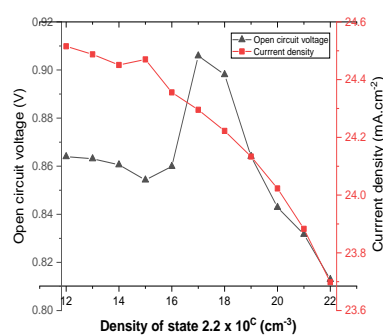


Figure 12. The dependence open circuit voltage and current density on the density of states (conduction band) for the CZCTS.

4. Conclusions

Finally, it has been shown that Cu₂Zn_{1-x}Ca_xSnS₄ can be synthesized and characterized. For the first time, Ca²⁺ has been used to tune the presence of Zn²⁺ in CZTS thin films has been demonstrated. In the visible and near-infrared spectrums, the alloys performed better in transmittance. As a result, the alloy is a wide bandgap (WBG) semiconductor with an optical bandgap of 3.84–4.04 eV. This energy shift is consistent with the energy gap with the behavior of dopants, as reported in the literature. In this work, simple synthesis and deposition of CZCTS thin film are reported by spin coating technique on a glass substrate. The thin film's structures,

morphologies, and optics were also studied. The effect of annealing temperature on the system, morphologies, and optics are thus reported elsewhere.

Funding

This research received no external funding.

Acknowledgments

DR. Marc Burgelman and his research group at the University of Gents, Belgium, developed the Solar Cells Capacitance Simulator – 1D (SCAPS-1D) simulation tool and freely made it available to us to enable the photovoltaic optimization and simulation of optoelectronic device systems.

Conflicts of Interest

The authors declare no conflict of interest.

References

1. Tousif, M.N.; Ushan, M.N.R.; Joha, A.A.; Mohammad, S. A comprehensive study of CZTS solar cell simulation with ZnSe buffer layer. In: Proceedings of the 2017 IEEE Region 10 Humanitarian Technology Conference (R10-HTC). 21-23 Dec. 2017, **2017**; pp. 193-197, <https://doi.org/10.1109/R10-HTC.2017.8288936>.
2. Crovetto, A.; Cazzaniga, A.; Ettliger, R.B.; Schou, J.; Hansen, O. Optical properties and surface characterization of pulsed laser-deposited Cu₂ZnSnS₄ by spectroscopic ellipsometry. *Thin Solid Films* **2015**, *582*, 203-207, <https://doi.org/10.1016/j.tsf.2014.11.075>.
3. Kanjana, N.; Maiagree, W.; Poolcharuansin, P.; Laokul, P. Synthesis and characterization of Fe-doped TiO₂ hollow spheres for dye-sensitized solar cell applications. *Materials Science and Engineering: B* **2021**, *271*, <https://doi.org/10.1016/j.mseb.2021.115311>.
4. Zakrzewski, J.; Maliński, M.; Bachiri, A.; Strzałkowski, K. Photothermal determination of the optical and thermal parameters of Cd_xZn_{1-x}Se mixed crystals. *Materials Science and Engineering: B* **2021**, *271*, <https://doi.org/10.1016/j.mseb.2021.115305>.
5. Akinrinola, O.; Awodugba, A.; Momodu, J.; Awodele, M.; Akinrinola, O.; Ibiyemi, A. On the Capacitance Spectroscopy of Cu₂ZnSnS₄ Typed Solar Cells Anisotype Heterojunction by SCAPS-1D. *Int. J. Eng. Technol.* **2021**, *6*, 37-44, <https://doi.org/10.19072/ijet.627225>.
6. Mygmarsereejid, P.; Ingram, M.; Batmunkh, M.; Zhong, Y.L. Doping Strategies in Sb₂S₃ Thin Films for Solar Cells. *Small* **2021**, *17*, 1-17, <https://doi.org/10.1002/sml.202100241>.
7. Emrani, A.; Vasekar, P.; Westgate, C.R. CZTS solar cells with 5.75% efficiency using sputtered precursors. Conf. Rec. IEEE Photovolt. Spec. Conf. **2013**; pp. 2545-2547, <https://doi.org/10.1109/PVSC.2013.6744993>.
8. Dorranean, D.; Dejam, L.; Mosayebian, G. Optical characterization of Cu₃N thin film with Swanepoel method. *Journal of Theoretical and Applied Physics* **2012**, *6*, <https://doi.org/10.1186/2251-7235-6-13>.
9. Selvan, B.K.; Thiagarajan, K.; Das, S.; Jaya, N.; Jabasingh, S.A.; Saravanan, P.; Rajasimman, M.; Vasseghian, Y. Synthesis and characterization of nano zerovalent iron-kaolin clay (nZVI-Kaol) composite polyethersulfone (PES) membrane for the efficacious As₂O₃ removal from potable water samples. *Chemosphere* **2022**, *288*, <https://doi.org/10.1016/j.chemosphere.2021.132405>.
10. Toma, F.T.Z.; Rahman, M.; Hussain, K.M.A.; Das, H.; Khan, M. Effect of the Annealing Temperature on CdS Nanoparticles Synthesized by Chemical Precipitation Technique and also Characterized for its Potential Technological Applications. *STM Journals* **2021**, *23*, 20-28.
11. Toma, F.T.Z.; Hussain, K.M.A.; Rahman, M.S.; Ahmed, S. Preparation and characterization of CdS thin film using chemical bath deposition (CBD) technique for solar cell application. *World Journal of Advanced Research and Reviews: an International Journal* **2021**, *12*, 629-633, <https://doi.org/10.30574/wjarr.2021.12.3.0746>.
12. Kadhim, A.K.; Abd Ali, A.I.; Mohammad, M.R. Preparation and Characterization of Electron Transfer Layer for Perovskite Solar Cells. *Journal of Applied Sciences and Nanotechnology* **2021**, *1*, 58-63, <https://doi.org/10.53293/jasn.2021.3521.1025>.
13. Borzdun, N.I.; Ramazanov, R.R.; Glova, A.D.; Larin, S.V.; Lyulin, S.V. Model Carboxyl-Containing Asphaltenes as Potential Acceptor Materials for Bulk Heterojunction Solar Cells. *Energy & Fuels* **2021**, *35*, 8423-8429, <https://doi.org/10.1021/acs.energyfuels.1c00253>.

14. Rabaia, M.K.H.; Abdelkareem, M.A.; Sayed, E.T.; Elsaid, K.; Chae, K.-J.; Wilberforce, T.; Olabi, A.G. Environmental impacts of solar energy systems: A review. *Science of The Total Environment* **2021**, *754*, <https://doi.org/10.1016/j.scitotenv.2020.141989>.
15. Isiyaku, A.K.; Ali, A.H.; Nayan, N. Effects of Laser Radiation on the Optical and Electrical Properties of ITO Thin Films Deposited by RF Sputtering. *Univers. J. Electr. Electron. Eng.* **2019**, *6*, 1-6, <https://doi.org/10.13189/ujeee.2019.061601>.
16. Younis, N.; Abd-Elrahman, M.I.; Afify, N.; Abu El-Fadl, A.; Abu-Sehly, A.A. Structural, optical and magnetic characterizations of nanoparticles spinel Zn(1-x)MxAl2O4 (M = Co and Ni) synthesized by microwave combustion method. *Materials Science and Engineering: B* **2021**, *271*, <https://doi.org/10.1016/j.mseb.2021.115316>.
17. Dubey, R.S.; Jadkar, S.R.; Bhorde, A.B. Synthesis and Characterization of Various Doped TiO2 Nanocrystals for Dye-Sensitized Solar Cells. *ACS Omega* **2021**, *6*, 3470-3482, <https://doi.org/10.1021/acsomega.0c01614>.
18. Bhat, T.S.; Bhogale, S.B.; Patil, S.S.; Pisal, S.H.; Phaltane, S.A.; Patil, P.S. Synthesis and characterization of hexagonal zinc oxide nanorods for Eosin-Y dye sensitized solar cell. *Materials Today: Proceedings* **2021**, *43*, 2800-2804, <https://doi.org/10.1016/j.matpr.2020.08.687>.
19. Katagiri, H.; Jimbo, K.; Maw, W.S.; Oishi, K.; Yamazaki, M.; Araki, H.; Takeuchi, A. Development of CZTS-based thin film solar cells. *Thin Solid Films* **2009**, *517*, 2455-2460, <https://doi.org/10.1016/j.tsf.2008.11.002>.
20. Suryawanshi, M.P.; Shin, S.W.; Ghorpade, U.V.; Gurav, K.V.; Hong, C.W.; Patil, P.S.; Moholkar, A.V.; Kim, J.H. Improved solar cell performance of Cu2ZnSnS4 (CZTS) thin films prepared by sulfurizing stacked precursor thin films via SILAR method. *Journal of Alloys and Compounds* **2016**, *671*, 509-516.
21. Diwate, K.; Mohite, K.; Shinde, M.; Rondiya, S.; Pawbake, A.; Date, A.; Pathan, H.; Jadkar, S. Synthesis and Characterization of Chemical Spray Pyrolysed CZTS Thin Films for Solar Cell Applications. *Energy Procedia* **2017**, *110*, 180-187, <https://doi.org/10.1016/j.egypro.2017.03.125>.
22. Suryawanshi, M.P.; Agawane, G.L.; Bhosale, S.M.; Shin, S.W.; Patil, P.S.; Kim, J.-H.; Moholkar, A.V. CZTS based thin film solar cells: a status review. *Materials Technology* **2013**, *28*, 98-109.
23. Olgar, M.A. Optimization of sulfurization time and temperature for fabrication of Cu2ZnSnS4 (CZTS) thin films. *Superlattices and Microstructures* **2019**, *126*, 32-41, <https://doi.org/10.1016/j.spmi.2018.12.012>.
24. Lin, Y.-P.; Chi, Y.-F.; Hsieh, T.-E.; Chen, Y.-C.; Huang, K.-P. Preparation of Cu2ZnSnS4 (CZTS) sputtering target and its application to the fabrication of CZTS thin-film solar cells. *Journal of Alloys and Compounds* **2016**, *654*, 498-508, <https://doi.org/10.1016/j.jallcom.2015.09.111>.
25. Wu, S.H.; Shih, C.F.; Pan, H.C.; Wang, Y.Y.; Chen, H.M.; Wu, C.S. Investigation of vulcanization of non-crystalline Cu2ZnSnS4 nano-particles. *Thin Solid Films* **2013**, *544*, 19-23, <https://doi.org/10.1016/j.tsf.2013.05.119>.
26. Cormier, P.A.; Snyders, R. One-step synthesis of Cu2ZnSnS4 thin films by reactive magnetron co-sputtering. *Acta Materialia* **2015**, *96*, 80-88, <https://doi.org/10.1016/j.actamat.2015.06.001>.
27. Ibiyemi, A.A.; Awodugba, A.O.; Akinrinola, O.; Faremi, A.A. Zinc-doped CdS nanoparticles synthesized by microwave-assisted deposition. *Journal of Semiconductors* **2017**, *38*, <https://doi.org/10.1088/1674-4926/38/9/093002>.
28. Ansari, M.Z.; Khare, N. Effect of intrinsic strain on the optical band gap of single phase nanostructured Cu2ZnSnS4. *Materials Science in Semiconductor Processing* **2017**, *63*, 220-226, <https://doi.org/10.1016/j.mssp.2017.02.011>.
29. Amole, S.; Awodele, M.K.; Adedokun, O.; Jain, M.; Awodugba, A.O. Sol-Gel Spin Coating Synthesis of TiO2 Nanostructure and Its Optical Characterization. *Journal of Materials Science and Chemical Engineering* **2019**, *7*, 23-34, <https://doi.org/10.4236/msce.2019.76003>.
30. Suresh, R.; Ponnuswamy, V.; Mariappan, R. Effect of annealing temperature on the microstructural, optical and electrical properties of CeO2 nanoparticles by chemical precipitation method. *Applied Surface Science* **2013**, *273*, 457-464, <https://doi.org/10.1016/j.apsusc.2013.02.062>.
31. Vidya, Y.S.; Anantharaju, K.S.; Nagabhushana, H.; Sharma, S.C.; Nagaswarupa, H.P.; Prashantha, S.C.; Shivakumara, C.; Danithkumar. Combustion synthesized tetragonal ZrO2: Eu3+ nanophosphors: Structural and photoluminescence studies. *Spectrochimica Acta Part A: Molecular and Biomolecular Spectroscopy* **2015**, *135*, 241-251, <https://doi.org/10.1016/j.saa.2014.06.151>.
32. Paquin, F.; Rivnay, J.; Salleo, A.; Stingelin, N.; Silva-Acuña, C. Multi-phase microstructures drive exciton dissociation in neat semicrystalline polymeric semiconductors. *Journal of Materials Chemistry C* **2015**, *3*, 10715-10722, <https://doi.org/10.1039/C5TC02043C>.
33. Li, Y.; Chen, J.; Ma, J. Properties of Cu2ZnSnS4 (CZTS) thin films prepared by plasma assisted co-evaporation. *Journal of Materials Science: Materials in Electronics* **2015**, *26*, 6546-6551, <https://doi.org/10.1007/s10854-015-3251-5>.
34. Zhang, X.; Fu, E.; Wang, Y.; Zhang, C. Fabrication of Cu2ZnSnS4 (CZTS) Nanoparticle Inks for Growth of CZTS Films for Solar Cells. *Nanomaterials* **2019**, *9*, 1-10, <https://doi.org/10.3390/nano9030336>.
35. Goktas, A.; Modanlı, S.; Tumbul, A.; Kilic, A. Facile synthesis and characterization of ZnO, ZnO:Co, and ZnO/ZnO:Co nano rod-like homojunction thin films: Role of crystallite/grain size and microstrain in

- photocatalytic performance. *Journal of Alloys and Compounds* **2022**, 893, <https://doi.org/10.1016/j.jallcom.2021.162334>.
36. Abd El Halim, B.; Mahfoud, A.; Mohammed Elamine, D. Numerical analysis of potential buffer layer for Cu₂ZnSnS₄ (CZTS) solar cells. *Optik* **2020**, 204, 1–7, <https://doi.org/10.1016/j.ijleo.2019.164155>.
37. Verma, P.; Ubaid, J.; Varadarajan, K.M.; Wardle, B.L.; Kumar, S. Synthesis and Characterization of Carbon Nanotube-Doped Thermoplastic Nanocomposites for the Additive Manufacturing of Self-Sensing Piezoresistive Materials. *ACS applied materials & interfaces* **2022**, 14, 8361-8372, <https://doi.org/10.1021/acsami.1c20491>.
38. Nisar, A.; Saeed, M.; Muneer, M.; Usman, M.; Khan, I. Synthesis and characterization of ZnO decorated reduced graphene oxide (ZnO-rGO) and evaluation of its photocatalytic activity toward photodegradation of methylene blue. *Environmental Science and Pollution Research* **2022**, 29, 418-430, <https://doi.org/10.1007/s11356-021-13520-6>.